# Supporting Information for "Martian Eolian Dust Probed by ChemCam"

**J. Lasue[1], A. Cousin[1], P.-Y. Meslin[1], N. Mangold[2], R.C. Wiens[3], G. Berger[1], E. Dehouck[4], O. Forni[1], W. Goetz[5], O. Gasnault[1], W. Rapin[6], S. Schroeder[7], A. Ollila[3], J. Johnson[8], S. Le Mouélic[2], S. Maurice[1], R. Anderson[9], D. Blaney[10], B. Clark[11], S.M. Clegg[12], C. d'Uston[1], C. Fabre[13], N. Lanza[3], M. B. Madsen[14], J. Martin-Torres[15], N. Melikechi[16], H. Newsom[17], V. Sautter[18]and M.P. Zorzano[15]**

[1]IRAP, Université de Toulouse, CNES, CNRS, UPS, Toulouse, France
[2]LPGN, CNRS UMR 6112, Université de Nantes, France
[3]ISR, MS D466, Los Alamos National Laboratory, Los Alamos, NM 87545, USA
[4]Université de Lyon, UCBL, ENSL, CNRS, LGL-TPE, 69622 Villeurbanne, France
[5]Max-Planck-Institut für Sonnensystemforschung, D - 37077 Göttingen, Germany
[6]CalTech, JPL, Los Angeles, CA, USA.
[7]DLR, Berlin, Germany
[8]Johns Hopkins University APL, Laurel, MD, USA
[9]USGS, Flagstaff, AZ, USA
[10]NASA JPL, Pasadena, CA, USA
[11]Space Science Institute, Boulder, CO, USA
[12]C-PCS, MS J565, Los Alamos National Laboratory, Los Alamos, NM 87545, USA
[13]GeoRessources, Lorraine University, CNRS, Vandoeuvre, FR-54500, France
[14]Niels Bohr Institute, Copenhagen, Denmark
[15]DST, Luleå University of Technology, Kiruna, Sweden
[16]U. Massachusetts Lowell, Lowell, MA, USA
[17]U. New Mexico, Albuquerque, NM, USA
[18]IMPMC, Muséum d'Histoire Naturelle, Paris, France
[19]Centro de Astrobiología (INTA-CSIC), Torrejón de Ardoz, Madrid, Spain

## Contents



Corresponding author: J. Lasue, `jlasue@irap.omp.eu`

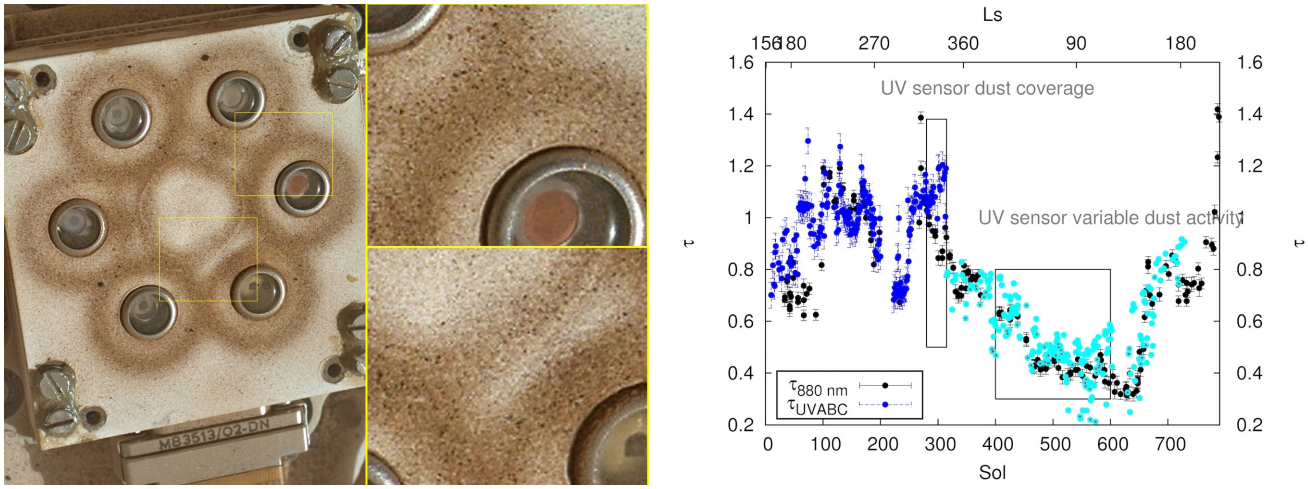


**Figure S1.** Evolution of dust cover on the UV sensors of MSL with time. (Left) Sol 323 MAHLI image of the UVS, taken after the passage of the regional dust storm. The image shows, in addition to the increased thickness of the dust that sticks to the magnetic rings, a thin cover of dust on the window of each photodiode. This thin cover induces a systematic reduction in the transmittance of the window. In the zoom in of the picture, different populations of dust grains with various colors can clearly be seen and show a mixing of dust particles deposited. (Right) Atmospheric opacity during the first 600 sols, comparison of the UV sensor and Mastcam derived opacity. After sol 300 the UV sensor was partially degraded by the dust deposited on the field-of-view of the photodiodes. The dust is strongly absorbing in the UV and a fine layer of a few microns affects the transmittance of the window of the sensor, the reduced incident irradiance is corrected by an offset of -0.35 and is shown by the light blue data points.

## Text S1.

Figure S1 describes the deposition of dust particles on MSL and the effect of a regional dust storm detected by the Rover Environmental Monitoring Station (REMS) onboard MSL. After the passage of the regional dust storm, the thickness of the dust that sticks to the magnetic rings surrounding the REMS UV sensors has increased and a thin cover of dust can be seen on the window of each photodiode. On Figure S1.a, one can see the mixture of different populations of grains deposited over the sensor head, with large to small and dark to light-colored grains. This dust cover induces a systematic reduction in the transmittance of the window since that event, which can be seen in the atmospheric opacity, $\tau$, measured during the first 600 sols by the UV sensor and Mastcam. After sol 300 the UV sensor was partially degraded by the dust deposited on the

field-of-view of the photodiodes. The dust is strongly absorbing in the UV and a fine layer of a few microns affects the transmittance of the window of the sensor, in this case reducing the incident irradiance. The UV sensor transmittance degradation factor is calculated by comparing the UV and MastCam in observations where the maximum UV diffuse irradiance is lower than 12% of the maximal global irradiance. For the example shown in Figure S1.b this provides an estimate to the transmittance degradation by an offset of -0.35. The data that are used as reference for recalibration (those with $< 12\%$ of diffuse irradiance) are marked in red.

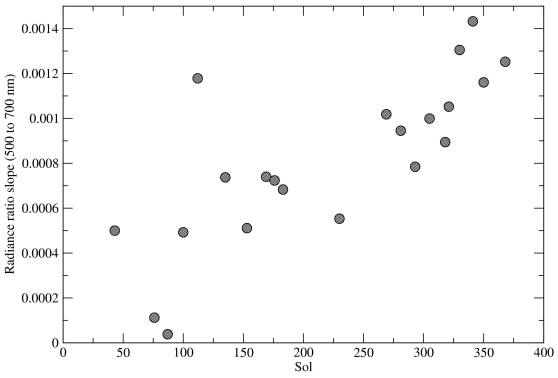


**Figure S2.** Radiance ratio slope between 500nm and 700nm in the VNIR passive spectra of ChemCam CCCT 11 as a function of the time during the first 360 sols. The increase of this ratio with time indicates continuous reddening of the rover surface on Mars due to dust deposition.

## Text S2.

ChemCam passive spectroscopy can also be used to monitor dust deposition. In this case, the calibration is done by comparison with the CCCT 11 which is a flat and white rover surface area located between the CCCTs. Figure S2 illustrates the change in reflectance spectra of the calibration targets of ChemCam on-board MSL using the radiance ratio slope between 500nm and 700nm as a proxy for the spectral reddening. The radiance ratio increases with time indicating a reddening of the rover paint with time due to continuous deposition of eolian dust particles on its surface. The deposition rate on the rover turns out to be relatively linear, particularly between sols 200 and 360, when the rover was motionless.

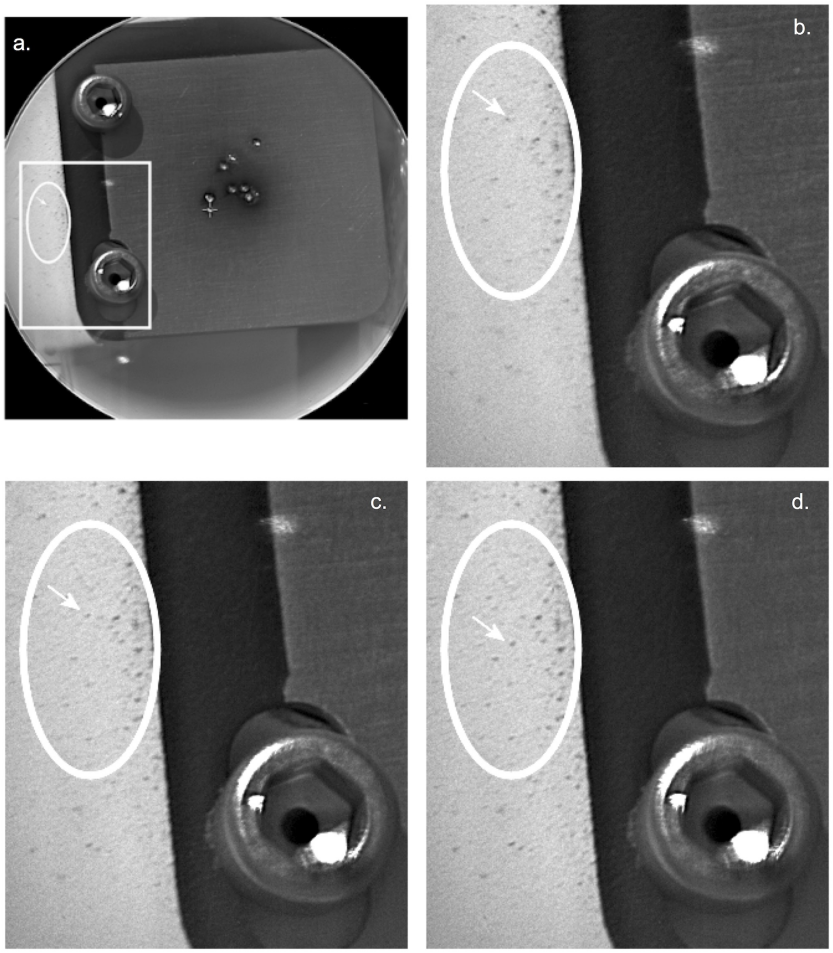


**Figure S3.** a) ChemCam RMI image of fine dust covering the ChemCam calibration target plate on sol 30 (CR0_401485256EDR_F0042002CCAM02045). Large particles visible on the image (sizes around 100 microns) are mostly aggregated clumps of smaller size dust grains. b-c-d) Set of three RMI images of the Titanium CCCT taken on sol 30, 69 seconds apart, showing a 100 micron dust clump move on the surface of the target, shown by white arrows. (CR0_400155651PRC_F0040000CCAM03030; CR0_400155720PRC_F0040000CCAM03030; CR0_400155789PRC_F0040000CCAM03030)

## Text S3.

As shown in Figure S3, a cover of very small dust particles was already present on the ChemCam calibration target plate after 30 sols (martian days) on the surface of Mars. The pixel scale of the RMI at this distance (1.56 m) is about 33 $\mu$m, and the large dark clumps visible on the image are mostly aggregates of smaller dust-size particles. The fact that these particles are very easily mobilized by eolian processes is demonstrated by the

fact that we can follow such a clump of dust as it moves near the surface of the Titanium calibration target on sol 30. The black dot (highlighted by the white arrows on the images) is about 100 microns in size and moves by about 1 mm in 140 seconds, probably under the influence of the wind.

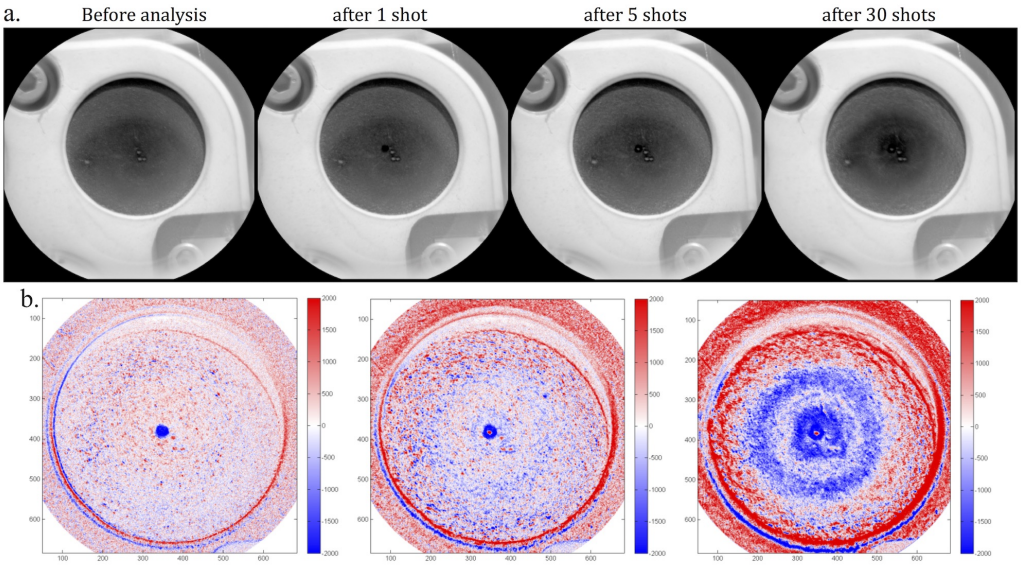


**Figure S4.** a. Set of 4 RMI images taken on sol 359 on the graphite CCCT 5 separated by ≈200 seconds each. The sequence of analysis by ChemCam was to take a first RMI image, then do a 30-shot sequence with an RMI image after 1 shot, 5 shots and 30 shots respectively. The radial motion of the dust particles covering the calibration target is clearly visible in the RMI images. (CR0_429357469EDR_F0120000CCAM02359, CR0_429357673EDR_F0120000CCAM02359, CR0_429357961EDR_F0120000CCAM02359, CR0_429358160EDR_F0120000CCAM02359). b. Difference images between the initial RMI image and the images (panel a) taken after 1 shot, 5 shots and 30 shots respectively. The central LIBS spot is clearly visible after the first shot and a dust-cleaned central area about 1cm in diameter is clearly visible after 30 shots.

## Text S4.

Figure S4a demonstrates in a different way the mobility of the dust deposited on the ChemCam calibration targets. The figure represents a sequence of active LIBS analyses on the graphite calibration target taken on sol 359. In that observation, the 30 shots that were typically taken in succession at 3 Hz were split into 3 sequences of 1, 4 and 25 shots. An RMI image was taken before and after the first shot, after 5 shots and af-

ter 30 shots on the target. Because the previous LIBS measurements were taken on sol 192, the initial scene represented a surface for which dust had a chance to deposit over 167 sols. The motion of the dust particles mobilized by the expanding LIBS plasma shockwave is clearly visible, with dust particles rippling away radially from the LIBS ablation spot. Figure S4b represents the differences between each image and the initial RMI taken before the analysis sequence, highlighting in color the effect of dust movement. The central LIBS spot is clearly visible and mostly cleared of dust after the first shot (diameter of ≈350 $\mu$m at 1.59 m). Then repetitive LIBS plasma expansions lead to a larger area of the CCCT5 being cleared of dust. After 30 shots on target, an area of about 1 cm diameter has been cleared of dust. This corresponds approximately to the maximum expansion diameter of the LIBS plasma under Mars conditions as analyzed in the laboratory.

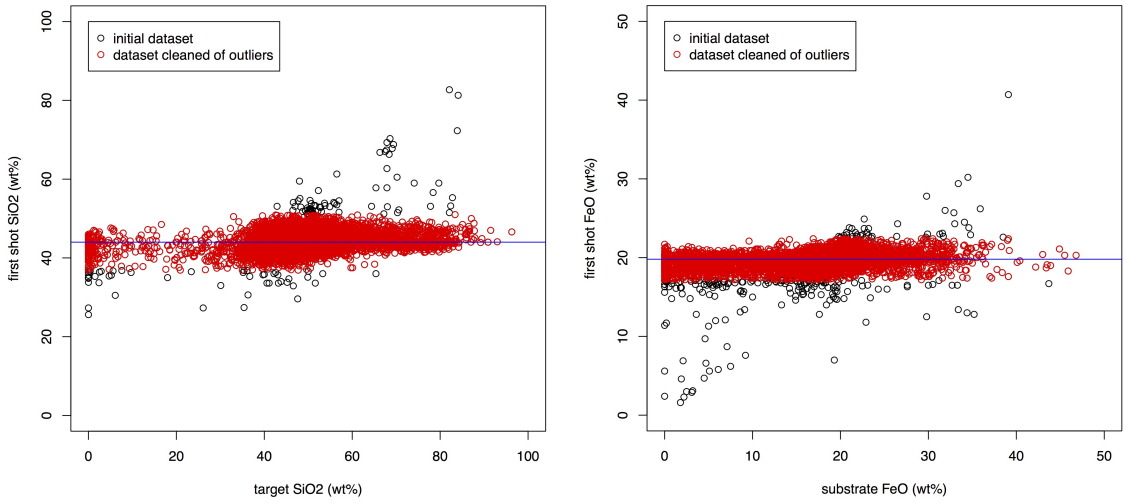


**Figure S5.** Plot of the variability of the first shot composition as a function of the underlying target composition for the $SiO_2$ and the FeO contents. The first shot composition is practically independent of the underlying target composition. The horizontal line correspond to the median value after outliers removal.

## Text S5.

Figure S5 compares the first shot composition to the underlying target composition for the $SiO_2$ and the FeO contents. The first shot composition is practically inde-

pendent of the underlying target composition. Therefore, the first ChemCam shots probe a material which is different from any target analyzed on Mars and is clearly reproducible over time. The horizontal line correspond to the median value after outliers removal from the dataset. This median value gives the estimate of the composition of the dust.

## Text S6.

Figure S6 compares the three ChemCam spectral ranges spectra from the dust (median of the first shots over 1600 sols) and the median spectra for the Aeolis Palus soils and the Bagnold Dunes. The three spectra appear very similar for all major elements and also minors elements. This indicates possible relationships between the materials. Similarities, differences and their consequences are discussed in details in the main text of the manuscript.

## Text S7.

Figures S7 compares the volatiles and minor elements contents between the median dust spectrum, taken from the first shots analysis, and the median Aeolis Palus soils and Bagnold Dunes spectra. Picrite is a ChemCam calibration target depleted in volatiles and NAHS is a ChemCam calibration target depleted in Cr.

Figures S7a and S7b demonstrate the presence of S and Cl in the dust spectrum, the soils and the sand dunes. These elements are notably difficult to detect with the LIBS technique and their limit of detection is at the level of several wt%. The fact that the lines start to be detected indicates their enhancement in the dust as compared to the typical local rocks analyzed at Gale crater. The Cl emission line appears weaker in the dust as compared to the soils and dunes. Figures S7c and S7d illustrate the hydrogen and lithium lines intensities which are at similar levels between the dust, the soils and the dunes. Finally, Figure S7e indicates a slight enrichment in the Cr content of the dust as compared to the soils and the dunes.

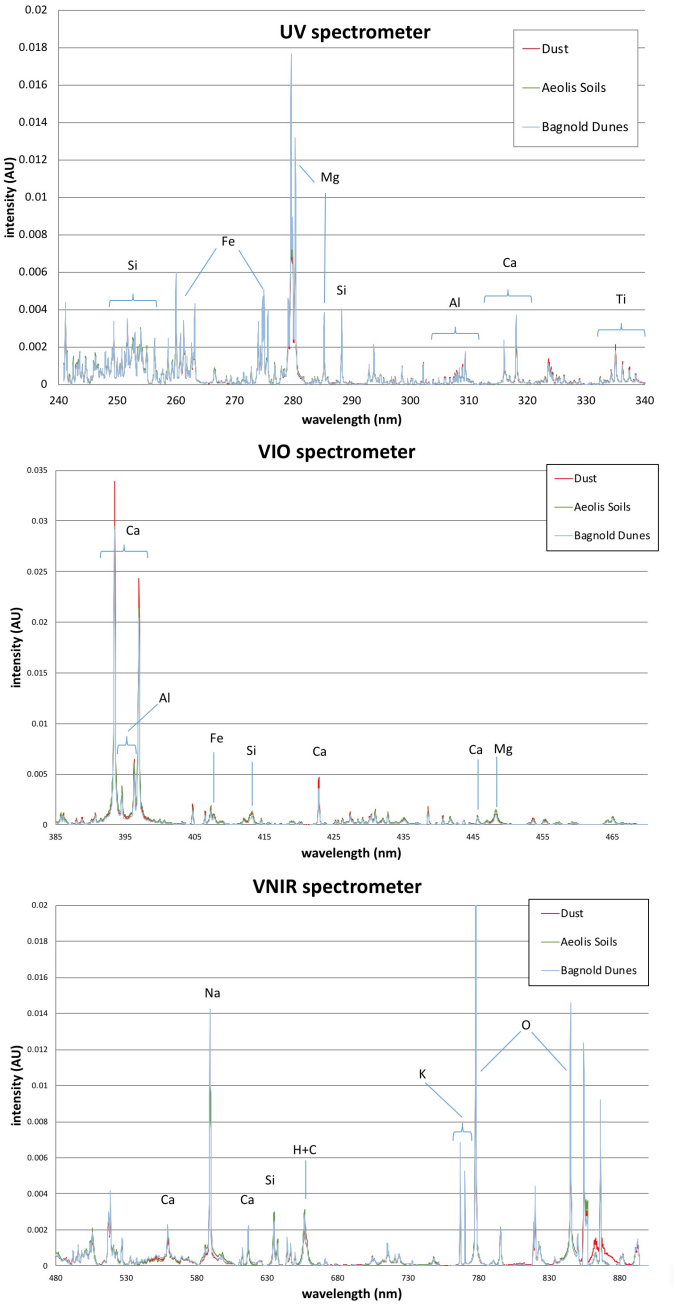


**Figure S6.** Comparison between the median LIBS spectra from the dust (median of the first shots over 1600 sols) and the median spectra for the Aeolis Palus soils and the Bagnold Dunes. The figure shows separately the three spectral ranges (a) UV; (b) VIO; (c) VNIR. The similarity in composition between the different materials is obvious, with very few peaks presenting detectable differences at this resolution. Elements represented by major emission lines in each spectral range are annotated.

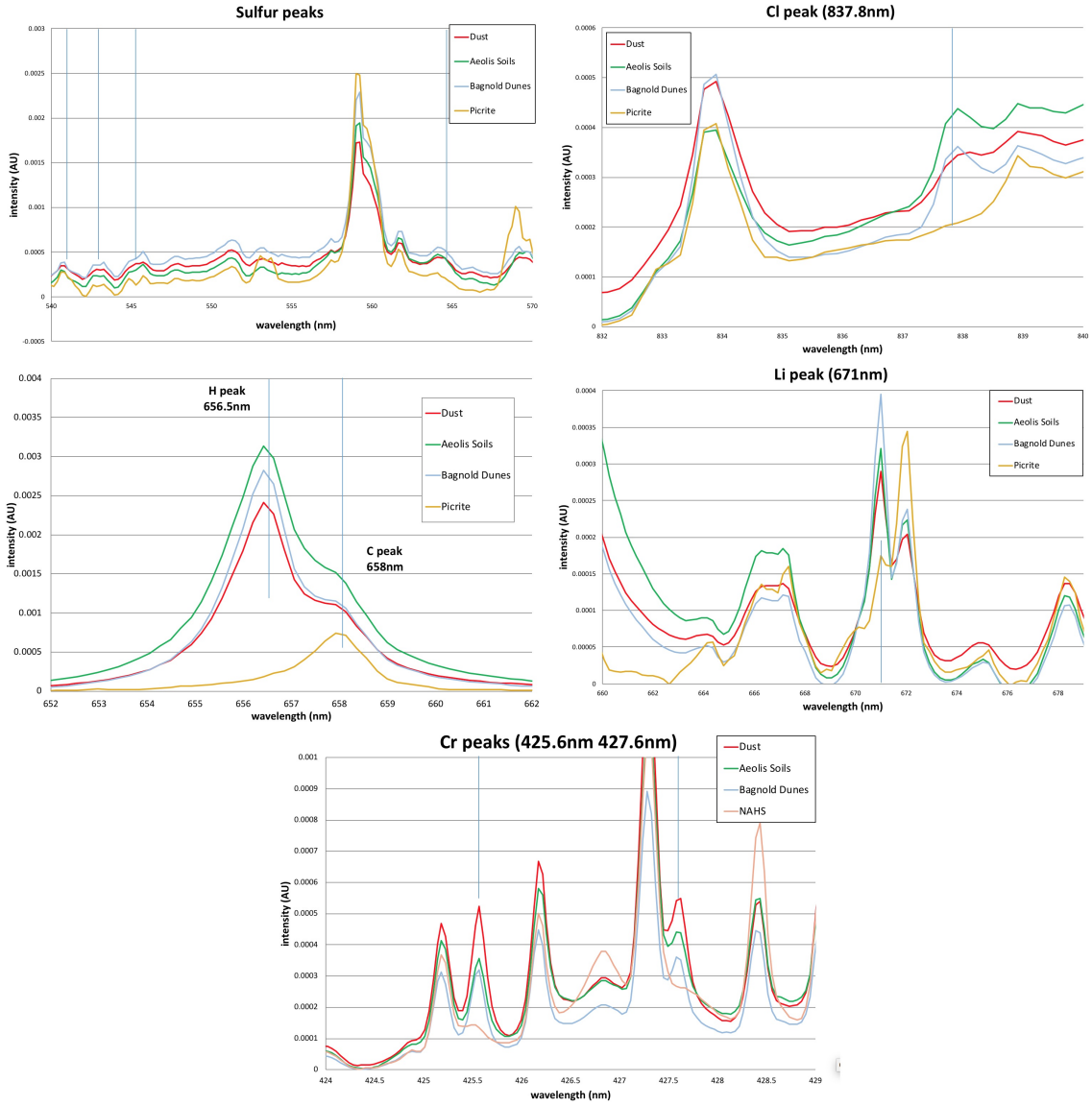


**Figure S7.** Comparison in the volatile and minor elements content between the median spectrum of the dust and the median spectra of Aeolis Palus soils and Bagnold dunes. Some ChemCam calibration targets depleted in the elements are added to the plots for comparison purposes. a. detection of the sulfur peaks in the dust; b. detection of the Cl peak in the dust; and comparison of the hydrogen (c) of the Li (d) and of the Cr (e) line intensities.